Characterizing surface finish and fatigue behavior in binder-jet 3D-printed nickel-based superalloy 625

Amir Mostafaei[1,†], S. Harsha Vardhan R. Neelapu[1], Cameron Kisailus[1], Lauren M. Nath[1], Tevis D.B. Jacobs[1], Markus Chmielus[1,*]

[1] Dept. of Mechanical Engineering and Materials Science, University of Pittsburgh, Pittsburgh, PA

[†] Current address: Dept. of Materials Science and Engineering, Carnegie Mellon University, Pittsburgh, PA,

* Corresponding author:
Email addresses: mostafaei@cmu.edu (Amir Mostafaei), chmielus@pitt.edu (Markus Chmielus).

Abstract

In this study, the fatigue properties of binder-jet 3D-printed nickel-base superalloy 625 were evaluated. Standard fatigue specimens were printed and sintered, then half of the samples were mechanically ground, while the other half were left in their as-sintered state. They were then characterized using micro-computed x-ray tomography, metallographic sample examination, and optical and stylus profilometry for surface topography. The micro-computed tomography observations showed that density of the as-printed sample was ~50%, while the sintered sample neared full densification (98.9 ± 0.3%) upon sintering at 1285 °C for 4 h in a vacuum atmosphere. The metallographic examination showed equiaxed grains. The roughness of the as-sintered samples was significant with an RMS roughness of $R_q = 1.39 \pm 0.20$ μm as measured over a line-scan of 5 mm, but this was reduced to $R_q = 0.47 \pm 0.02$ μm after mechanical grinding. All samples were tested to failure in fatigue, under fully-reversed tension-compression conditions. While the as-sintered samples showed poor fatigue properties compared to prior reports on cast and milled parts, the ground samples showed superior performance. Scanning electron microscopy observation was conducted on the fractured surfaces and showed that the samples underwent transgranular crack initiation, followed by intergranular crack growth and final failure. In the mechanically ground sample, hardness increased nearly two-fold up to 75 μm beneath the sample's surface and X-ray diffraction indicated an in-plane compressive stress, grain refinement, and micro-strain on the mechanically ground sample. The reduced roughness, surface hardening, and compressive stress resulted in increased fatigue life of the binder-jetted alloy 625.

Keywords: Additive manufacturing; Inconel 625; Sintering; Fatigue life; Fractography; Surface roughness; Hardness.

1. Introduction

Binder-jet 3D printing (BJ3DP) is a fast, low-cost process in which powder is deposited layer-by-layer, selectively joined in each layer with binder, and then sintered using a post-printing heat treatment to densify green parts [1,2]. Binder jetting uses inkjet printing technologies to bond the particles with the polymer binder in a layer-by-layer fashion, in contrast to laser-based [3,4] or electron-beam [5,6] additive manufacturing, which employ an energy source to completely or partially melt and subsequently fuse the particles. A primary drawback of these latter techniques is the uncontrolled thermal history and residual stresses that build up during printing [7–10]. Binder jetting [11,12] does not introduce residual stress during the printing process and enables uniform and highly controlled heating during the sintering step. It therefore results in parts with lower and more predictable residual stresses [1,13].

Nickel-based superalloys are in common use in the aerospace industry because of their excellent mechanical strength for room- or high-temperature applications, good surface stability, and resistance to high-temperature corrosion or oxidation [14,15]. Alloy 625 displays a useful combination of high yield strength and fatigue strength, as well as resistance to oxidation and corrosion in aggressive environments [15]. Alloy 625 has been used in many applications such as chemical, petrochemical, aerospace, and marine applications [16–21]. However, components with highly complex shapes made from this superalloy are either impossible or very expensive to produce through conventional machining [9]. BJ3DP is an alternative way to reduce machining and produce parts with complex internal and external geometries. Due to its large print rate, BJ3DP is ideally suited for low-volume manufacturing, particularly for high-cost materials [2], and has the flexibility to engineer microstructure and chemical composition [12–14].

Mechanical surface treatments play an important role in improving surface roughness and fatigue resistance by producing a compressive residual stress in the surface region of metallic parts [22–27]. The compressive stress results in a delayed crack initiation and retarded crack propagation. There has been only limited investigation into the fatigue life, crack propagation, and fracture toughness of additively manufactured alloy 625 [4,28,29]. It was reported that the fatigue life of the cast and additively manufactured parts is significantly lower compared to the wrought material [30]. While this report did not demonstrate the root cause of the lower performance, a different investigation into Ti-6Al-4V [31] demonstrated four key factors for fatigue performance: (1) residual stress, (2) microstructure, (3) porosity, and (4) surface finish. In this study, it was proposed that in the case of fusion-based additive manufacturing methods, residual stress is a primary issue that negatively affects fatigue life. The selective laser melted specimens exhibit larger degrees of tensile residual surface stresses resulting in a lower fatigue performance, while the electron beam melted specimens result in lower as-built residual stresses due to the higher build chamber temperature minimizing thermal gradients during deposition. The authors also showed differences in crack propagation between columnar or epitaxial grain morphologies. The presence of porosity or any internal defect due to unmelted powders negatively impacts the fatigue life because these

serve as stress concentrations and sites for initiation of fatigue cracks [32,33]. Similarly, the surface roughness and/or process-induced defects such as porosity after surface finishing are expected to drive premature fatigue crack initiation and failure [34]. Based on the alloy composition and manufacturing method, different surface treatments have been applied to improve surface roughness and relieve the residual stress caused during the printing process [20,21,23]. These four factors will be investigated in the present report as possible factors influencing fatigue performance.

The fatigue behavior of cast alloy 625 has been summarized in Refs. [4,30]. Despite some investigation into the fusion processes of metallic materials, there is little information on the fatigue behavior of BJ3DP parts made from metallic materials. While earlier BJ3DP studies [1,2,7,9–13,36–39] pertain to densification, microstructural analysis, hardness and a few investigations into tensile property characterization, the purpose of the present work is to evaluate the fatigue properties of alloy 625 created with BJ3DP. Specifically, samples in their as-sintered and mechanically ground state will be characterized (according to the four factors discussed in the previous paragraph), and tested in fatigue. An improved understanding of fatigue performance will guide the printing and post-processing of alloy 625 in real-world applications.

2. Materials and methods

Air-melted, nitrogen-atomized nickel-based alloy 625 powder was supplied by Carpenter Technology Corporation with the composition given in Table 1. Powder morphology and elemental composition analysis were performed with an SEM (JSM 6510, JEOL, Tokyo, Japan) equipped with energy dispersive X-ray spectroscopy (EDS). The particle size distribution was analyzed with a Microtrac S3500 tri-laser diffraction particle analyzer [40]. General morphology and internal porosity of the powder particles, and density of the as-printed and sintered samples were visualized with a micro-computed tomography (μCT) on small cylindrical (1 mm diameter) samples printed and sintered along with the fatigue samples. The size of these samples was chosen to accommodate the limited penetration depth of x-rays in fully dense alloy 625: 1.5-2 mm under present conditions. The μCT scanner (SkyScan1272, Bruker, Kontick, Belgium) was operated with 100 kV, 100 mA and a 0.11 mm Cu filter, averaging of 10 frames, angular range of 0°-180° with 0.2° steps and a pixel size of 1 μm. Fig. 1a illustrates the SEM image of the superalloy 625 powder used in the experiments. Additionally, μCT observation (Fig. 1b) indicated porosity within powder particles. It was seen in the μCT and SEM micrographs that alloy 625 powders had a spherical form. Fig. 1c illustrates the curve obtained from the particle size distribution analysis conducted by using Microtrac particle analyzer and results showed that the average powder size and particle size distribution were 32.0 μm and 18.6-44.2 μm, respectively (as reported in our earlier study in [10,13]).
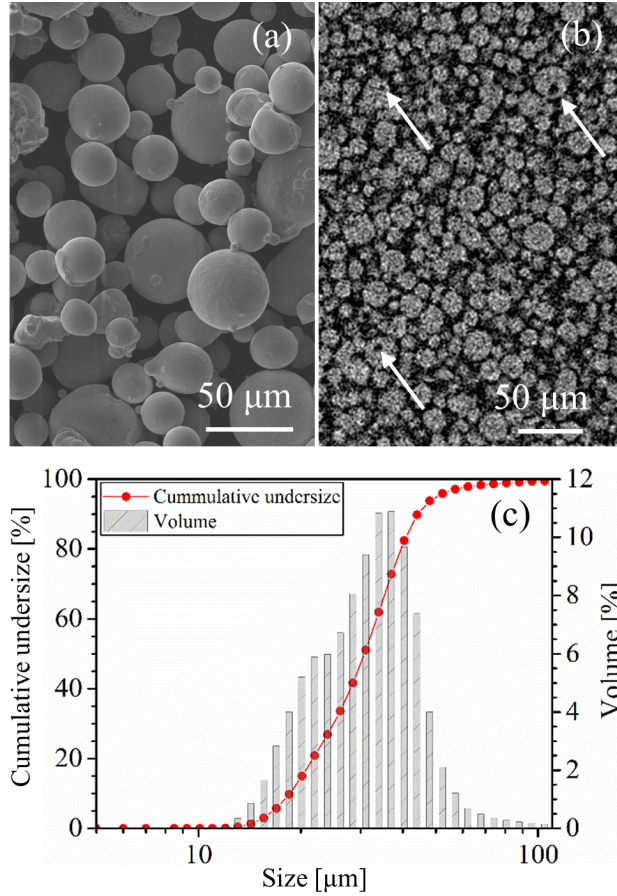
Fig. 1. (a) SEM and (b) µCT micrographs of the alloy 625 powder, illustrating powder morphology and internal porosity (indicated by arrows) of the feedstock powder. (c) The particle size distribution was measured using a laser particle size analyzer.

Table 1. Chemical composition of alloy 625 powder.

	Composition in atomic weight percent [wt.-%]									
Elements	Ni	Cr	Fe	Nb	Mo	Al	Ti	Co	Mn	Si
Nominal composition [13]	>58	20-23	<5	3.1-4.1	8-10	<0.4	<0.4	<1.0	<0.5	<0.5
Provided by manufacturer	Bal.	21.5	4.2	3.3	8.9	-	-	-	0.4	0.4
EDS analysis	Bal.	21.8	4.4	3.6	8.0	0.02	0.02	0.22	0.4	0.5

Fig. 2 shows schematic of the design used during printing as well as the representative fatigue-test samples. The orientation of the samples was laying flat along the platform, with their long axes parallel to the y-direction. Sixty samples were printed using an M-Flex ExOne binder jet printer with processing parameters as follows: binder saturation of 60%, layer thickness of 100 µm, recoat speed of 130 mm/s, oscillator speed of 2050 rpm, roller speed of 250 rpm, roller traverse speed of 15 mm/s, and drying speed of 17 mm/s [1,9]. The green parts were cured to improve strength of

the printed samples at 175 °C for 8 h in a JPW Design & Manufacturing furnace and then sintered in a Lindberg tube furnace in an alumina powder bed under vacuum at 1285 °C for 4 h. A sintering temperature above the liquidus line for this composition was chosen to ensure liquid-phase sintering. For half of the sintered fatigue samples, the curved surface of the test volume was mechanically ground using a rotary tool (Dremel 4000, Dremel, Racine, Wisconsin, USA). To improve consistency, all samples were ground in one sitting and by an experienced operator. Quality and consistency was confirmed via surface roughness measurements along eight directions on the test volumes via surface roughness measurements (not shown here).
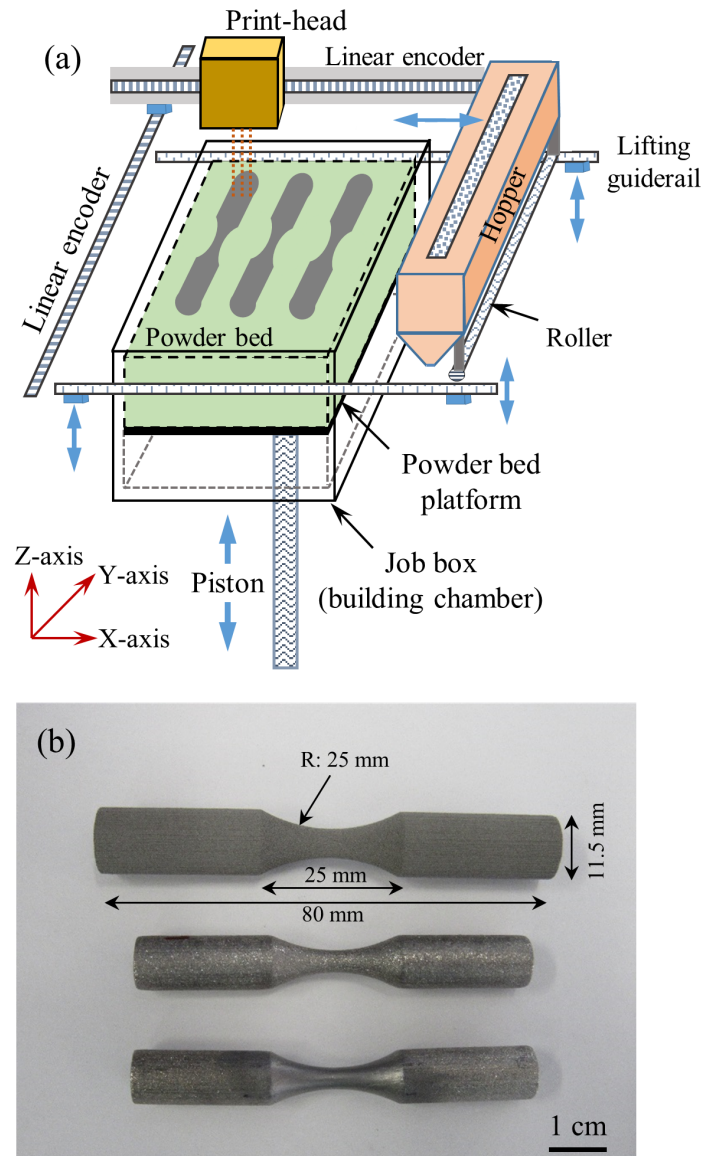

Fig. 2. (a) Schematic of the binder-jet 3D printing machine with the printing orientation during fabrication of the fatigue samples and (b) optical images representative samples in the as-printed (top), as-sintered (middle) and mechanically ground (bottom) condition. Dimensions of the printed samples are shown.

5

The samples were fatigue tested in air using a hydraulically driven load-frame (MTS 880, MTS, Eden Prairie, Minnesota, USA) under a stress-controlled, sinusoidal waveform with a tension-compression condition at R = -1 with 5 Hz and 7 Hz frequency (for the as-sintered and mechanically ground samples, respectively, frequency was increased to accommodate as many samples as possible, due to a larger variation in cycles to failure numbers) where $R = \sigma_{min}/\sigma_{max}$ and σ_{min} and σ_{max} are the applied minimum and maximum stresses, respectively. For the as-sintered condition, two samples were tested per stress level since cycle to failure numbers were similar; for the mechanically ground condition, three samples were tested per stress level, since there was more variation in the number of cycles to failure. The run-out limit was set to 10^7 cycles. Engineering stress values were selected between 175 MPa and 375 MPa with 25 MPa intervals. As presented in our earlier study [13], yield strength of the BJ3DP alloy 625 is 376 ± 14 MPa. For each specimen, the central diameter of the curved surface was measured in order to calculate the required force for each test condition. Before fatigue testing, some samples were sectioned for metallographic examination using SEM. After failure, SEM was used to observe the fracture surfaces.

Surface roughness profiles were measured using a stylus profilometer (Alpha-Step IQ, KLA-Tencor, Milpitas, California, USA). A 5-µm radius tip was used with a 16.5 mg load. Measurements were performed with a scan length of 5 mm, a scan rate of 10 µm/s, and a data sampling rate of 100 Hz. This yields points every 100 nm in lateral position. Scans were conducted parallel to the long axis of the sample at 10 different radial positions along the circumference. In all cases, the data is tilt-compensated by subtracting out the mean line, and also parabola-compensated to remove the contribution of overall sample geometry from the measurement of surface topography.

The surface morphology and roughness of the specimens were also analyzed by an optical profilometer (ContourGT, Bruker, Billerica, MA, USA). The print direction was determined by observing the horizontal print lines on the end of each sample. The flat sample end was then marked perpendicular and parallel to the print direction with the perpendicular direction being north (N) and south (S) and the parallel direction being east (E) and west (W). Each of these quadrants was bisected and respectively marked NE, NW, SE, SW for a total of 8 measurement directions. For each direction, a scan was performed with an objective lens with magnification of 5X, resulting in sample sizes of approximately 1 by 0.75 mm².

To evaluate the extent of sub-surface deformation and stress, microhardness testing was performed on cross-sections of the samples. Square coupons of material with dimensions of $10 \times 10 \times 5$ mm³ were printed and sintered under identical conditions as the fatigue samples, and subjected to identical mechanical grinding. The samples were then sectioned using a low-speed diamond saw

(Allied TechCut 4). The cross-section surface was ground (240 - 1200 grit SiC grinding paper) and polished (using first 1.0 μm and then 0.5 μm alumina particles). Then, the cross-section surfaces were subjected to Vickers microhardness testing using a Leco LM 800 Microhardness Tester under 25 and 50 gf loads with a dwell time of 10 s. Two replicates were performed at each of the two loads, for a total of four data sets per material. The lines of testing were performed at angles of 5° and 15° with respect to the original surface in order to improve depth resolution. Crystallography parameters were identified using an x-ray diffractometer (XRD, Bruker AXS D8 Discover) with Cu–Kα radiation (λ = 1.54 Å, 40 kV, 40 mA) with a step of 0.02°, a scan speed of 0.5 s/step and 2θ ranging from 35° to 95° at room temperature.

3. Results and discussion

3.1. Fatigue testing

The results of the fatigue tests are shown in Fig. 3 for the as-printed and mechanically ground samples, and they are compared for reference with the results from a prior fatigue investigation cast alloy 625 [8]. In the prior work, the specimens were cast, then machined with wire electrical discharge machining (EDM) and milling, and then mechanically ground. It was reported by Ayesta et al. [41] that the surface roughness obtained with wire electrical discharge machining was similar to that obtained with mechanical grinding, and it followed a random pattern, obtaining similar roughness values in any direction. Additionally, both processes showed a minimum heat affected layer. Therefore, the addition of EDM in the cast samples is unlikely to cause significant differences. The yield strength of the cast alloy 625 was reported as 350 MPa [8] and 351 MPa for the injection molded alloy 625 [42]. In our previous study on the binder jet printed parts made from nitrogen gas atomized alloy 625 powder, the yield strength value was found to be similar at 376 MPa [13]. Therefore, the limit of 375 MPa was selected for the maximum applied stress in this study. It was seen that the as-sintered samples failed far earlier than the cast samples [8], with up to one order of magnitude fewer cycles to failure. It is unsurprising that the unground as-sintered sample would show poorer performance than the ground cast samples; however, this result serves to underscore the low quality of the native surface finish of a binder-jetted part and the magnitude of its effect on performance. By contrast, the mechanically ground samples had superior fatigue life compared to both the cast alloy and as-sintered samples, again by up to one order of magnitude. Further, the mechanically ground samples that were tested below 300 MPa met the runout condition (10^7 cycles) and the testing was stopped. This indicates that the performance improvement at low stresses may be even better than is reflected in Fig. 3. Finally, it should be noted that the stress ratio (R) in the present study was -1, while the fatigue study of alloy 625 by Theriault [8] was conducted at R = 0.1. It is well known that tests performed at lower R values, and particularly negative values, result in lower fatigue life than those performed at higher R values [43]. Therefore, the performance of the present samples is even further superior to the cast alloy than is apparent in Fig. 3.
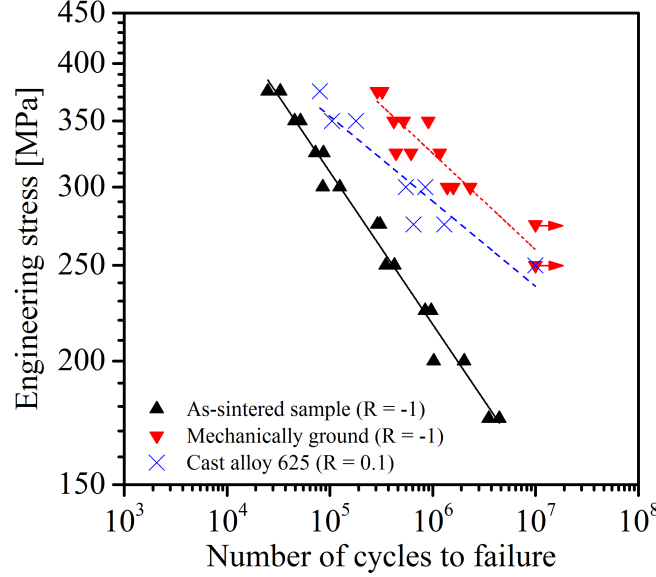
Fig. 3. Fatigue life data of the BJ3DP alloy 625 for the as-sintered condition (black) and after mechanical grinding (red). The horizontal arrows indicate that the runout condition of 10^7 cycles has been met and the test was stopped. For comparison, fatigue data is included from Ref. [8] for cast samples of alloy 625 ($f = 60$ Hz). In all cases, the experimental data has been fit with Eq. 1.

The experimental data were fit using the Basquin equation [44]:

$$\sigma_a = \sigma_f'\left(2N_f\right)^b \tag{1}$$

where σ_a is the stress amplitude (which is equal to the max stress in fully-reversed loading), N_f is the number of cycles to failure, and σ_f' and b are the fatigue strength coefficient and fatigue strength exponent, respectively. All datasets are reasonably well fit ($R^2 > 0.85$) with this power-law form. The resulting fatigue strength coefficients were $\sigma_f' = 781$, 747, and 764 MPa for the as-sintered, mechanically ground, and cast materials. The resulting fatigue strength exponents are $b = -0.15$, -0.10, and -0.09 for the as-sintered, mechanically ground, and cast materials, respectively. For most metals, b is in the range of -0.05 to -0.12, with typical values around -0.1 [45]. For a given value of σ_f', values of b that are closer to zero indicate less dependence on stress and superior fatigue performance. As noted, the mechanically ground samples experienced runout at low stresses and therefore were not tested to final failure. Larger values of N_f at low values of σ_a would further increase the best-fit exponent; therefore, the presently measured value of $b = -0.10$ for the mechanically ground sample represents a lower bound on this value. Overall, Fig. 3 demonstrates that the fatigue data are well fit by the Basquin equation and that the performance of the mechanically ground AM samples is superior to that of the cast and ball-milled parts.

Fig. 4 illustrates SEM micrographs of the overall fracture surfaces for selected samples. Fig. 4a$_2$ shows the fracture surface of the as-sintered sample at the applied stress value of 175 MPa failed

after 4.5×10^6 cycles with a transgranular surface area of 8.08 mm^2. By increasing the applied stress to 275 MPa, the fatigue life decreased to 3.1×10^5 cycles with the transgranular surface area of 5.48 mm^2 (Fig. 4b$_2$). At 375 MPa applied stress, the fatigue life decreased further to 2.5×10^4 cycles with the transgranular surface area of 2.79 mm^2 (Fig. 4c$_2$). The measured transgranular surface area clearly showed how the applied stress value affected the fracture surface as well as fracture mode. Finally, Fig. 4d$_2$ shows the fracture surface of a selected mechanically ground sample tested at 375 MPa, which experienced fatigue failure after 5.5×10^5 cycles and transgranular surface area of 9.50 mm^2. Supplementary Fig. 1 shows the fracture surface of the mechanically ground sample tested at 300 MPa, which experienced fatigue failure after 1.5×10^6 cycles with a fully transgranular fracture surface area. It was found that the same trend of decreasing transgranular fracture surface and increasing intergranular fracture surface has happened for the mechanically ground condition. In all cases, the crack initiated on the surface of the samples and failure took place near the area of the smallest diameter of the neck of the samples. No pore was seen on the micrographs indicating nearly full density of the BJ3DP parts. After crack initiation, the crack grew in a stage I crack growth mode as is indicated by the transgranular fracture surface. Stage I crack growth mainly progresses by slip plane cracking and was identified by the presence of facets at the initiation sites. Finally, the crack growth continued via intergranular fracture. The dash-line curves on the backscattered electron SEM micrographs show the approximate boundary between the fatigue crack initiation (transgranular crack growth) and intergranular fracture zones.
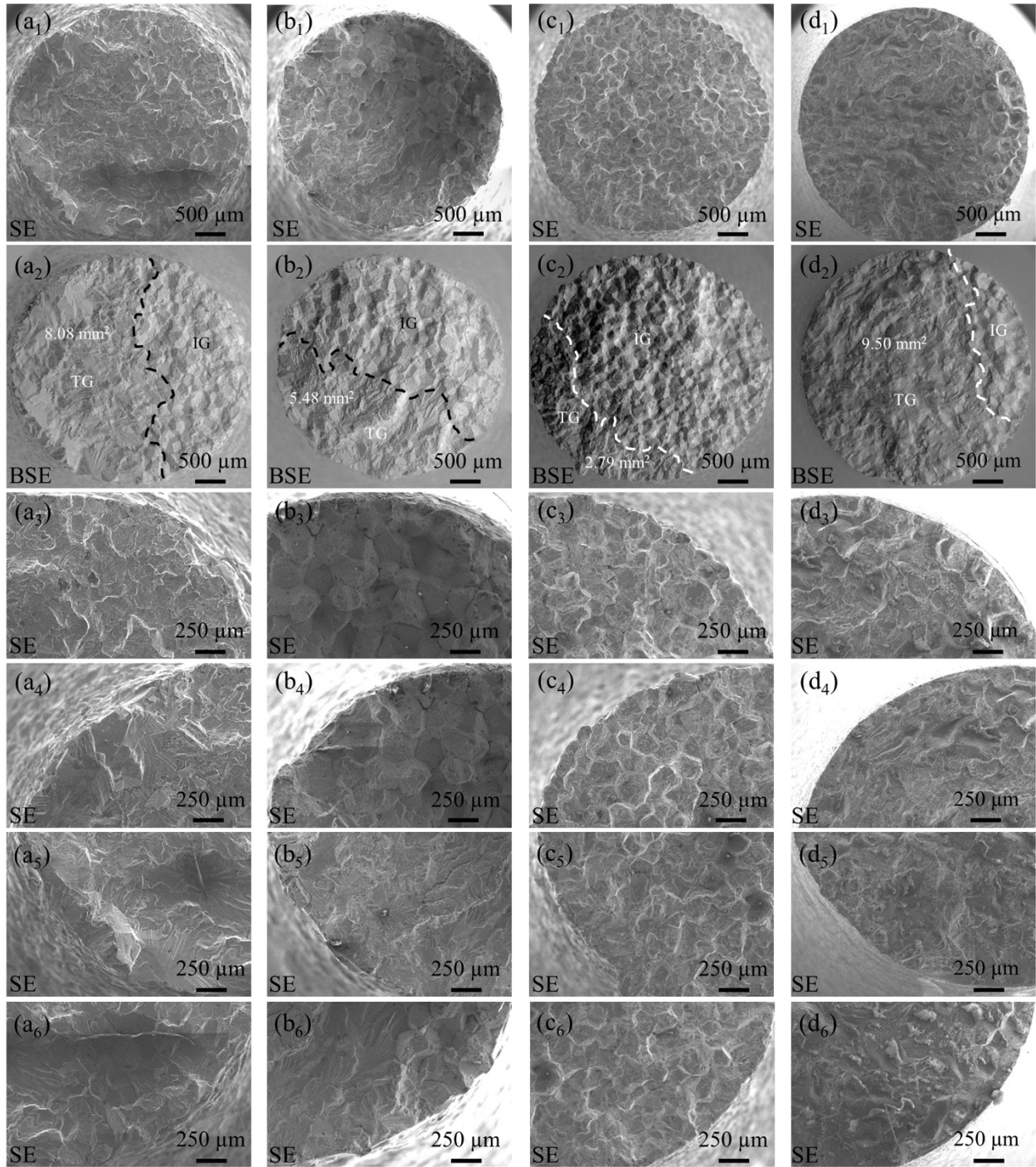
Fig. 4. Fatigue fracture, crack initiation and crack growth micrographs taken from the as-sintered samples at the applied stress value of (a) 175 MPa, (b) 275 MPa and (c) 375 MPa. (d) Selected fracture surface of the mechanically ground sample at the applied stress value of 375 MPa. Two different fracture modes are shown in BSE micrographs as transgranular (TG) and intergranular (IG) fatigue fracture failures. Different magnifications are used to indicate regions with different features, such as brittle and ductile fractures.

3.2. Materials characterization of the samples

Prior to fatigue testing, the samples were characterized using optical microscopy, scanning electron microscopy, and μCT for material properties, and then using stylus and optical profilometry for surface topography. Fig. 5 shows optical micrographs of the external surface of the samples. In Fig. 5a and Fig. 5a$_1$, printing layers (horizontal) and print direction (vertical) can be seen. After sintering (see Fig. 5b and Fig. 5b$_1$), neighboring powders joined to form larger grains on the outer surface. It is seen that deep valleys are possibly present on the surface. Fig. 5c and Fig. 5c$_1$ showed the sample surface after surface treatment indicating that the surface was smoother than the as-sintered sample.
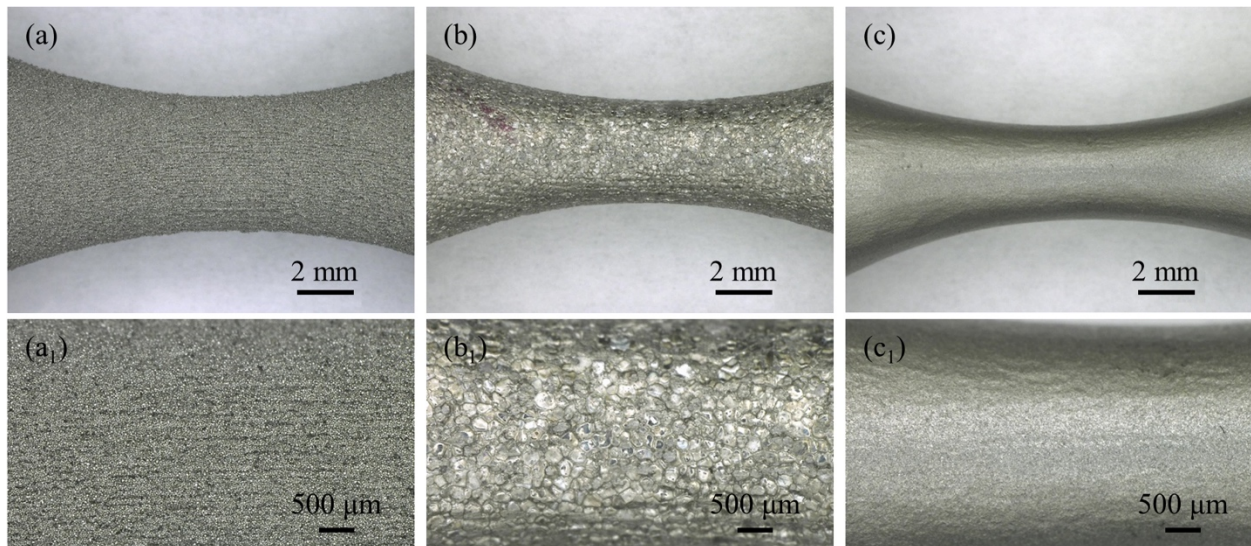

Fig. 5. Side-view optical micrographs taken from the surface of the fatigue samples (a,a$_1$) as-printed, (b,b$_1$) as-sintered, and (c,c$_1$) mechanically ground.

Fig. 6a illustrates the μCT shadow projection micrograph taken from the cylindrical sample before the sintering process. Layers with uniform thickness made from the metal powder were observed in Fig. 6a. The periodic variation in density within the layer plane detected in Fig. 6b is thought to be caused by the impact of binder droplets ejected from the print head nozzles during printing process (higher print head resolution with smaller nozzle and droplet size may prevent the formation of the periodic variation within each layer). The visibility of these regular layers in both the build direction and the layer plane of binder-jet 3D-printed parts using μCT is distinct and has been shown before [13]. Fig. 6c displays the μCT shadow projection taken from the same sample after the sintering process. The same samples that were used for μCT were also cross-sectioned (perpendicular to the powder bed plane) and polished and etched in order to take optical and SEM micrographs of internal features. The near-fully densified sample is illustrated in Fig. 6d. The SEM microstructural examination showed an equiaxed grain structure which may offer more resistance to cyclic deformation (Fig. 6d). Based on prior observation of similar materials (i.e. alloy 625, 16-

11

63 μm powder size range) and the random orientation of the powder feedstock, the grain structure is assumed to be isotropic [13]. Optical microscopy observations in Fig. 6e at the cross-section (perpendicular to the powder bed plane) of the printed coupon close to the surface of the sintered sample showed uniform density and grain size. The μCT shadow projection is dark after the sintering process at 1285 °C for 4 h, suggesting high density. Indeed, a density value of 98.9 ± 0.3% was computed using Archimedes and image analysis on sintered coupon samples with the same processing parameters. The dimensional change in the sample upon sintering was measured to be 17 ± 1%. These observations are in agreement with our previous studies in [1,9,10,13], which include additional information about the sintering conditions, microstructural development, mechanical properties and densification for binder-jet printing of alloy 625. Based on the examination using optical microscopy, scanning electron microscopy, and μCT, the better fatigue performance may be attributable to the removal of the outer layers. The topography of these outer layers was further studied using profilometry.
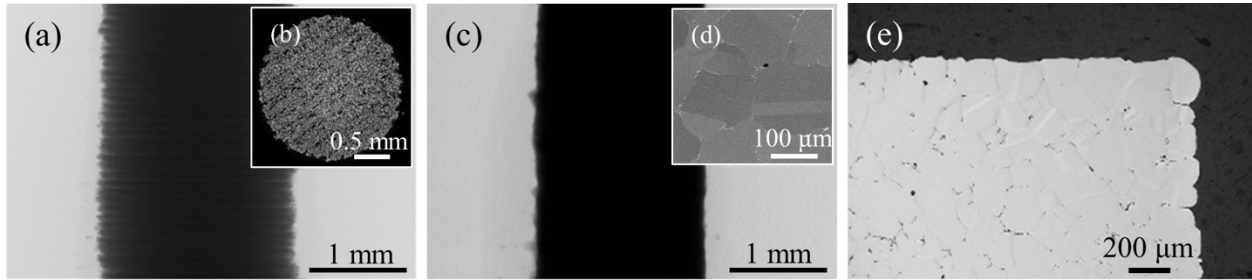

Fig. 6. (a) μCT shadow projection micrograph taken from the as-printed representative cylinder printed with the same powder and printing parameters. (b) μCT micrograph taken from same sample, indicating powder morphology and printing layers. (c) μCT shadow projection taken from the sintered representative cylinder. (d) SEM micrograph and (e) optical image taken from the sintered sample showing near-fully densified part.

The surface topography of the as-sintered and mechanically ground samples was measured using stylus and optical profilometry, as shown in Fig. 7. The extreme roughness of the as-sintered parts that was visually observable (Fig. 5b) is quantified in the topography characterization. In order to quantify the variation in roughness between the different surface conditions, two different metrics were compared: the root-mean-square height variation (often called h_{rms}) and the root-mean-square roughness (often called R_q). Both are computed using the same equation, but the former is applied directly to the measured height data (after line- and parabola-compensation, see Methods) and the latter is applied to the height data after the application of a Gaussian filter to remove the larger-scale features:

$$h_{rms} = \sqrt{\frac{1}{L}\int_0^L \left(h_{unfiltered}(x)\right)^2 \, dx} \tag{2a}$$

$$R_q = \sqrt{\frac{1}{L}\int_0^L \left(h_{filtered}(x)\right)^2 \, dx} \tag{2b}$$

where h is the height measured at position x over a scan length of L. These are numerically implemented using the trapezoidal rule. For the filtering, a Gaussian filter with a cut-off of 80 μm was applied, in accordance with ISO 4288. Using stylus profilometry, the RMS height variation was measured as h_{rms} = 24.77 ± 5.13 μm for the as-sintered sample and was reduced to h_{rms} = 3.76 ± 1.07 μm upon mechanical grinding. The measured values of RMS roughness were R_q = 1.39 ± 0.20 μm and R_q = 0.47 ± 0.02 μm, for the as-sintered and mechanically ground samples, respectively. Another metric used to quantify topography is average roughness (which typically scales with R_q), which was reduced upon grinding from R_a= 1.10 ± 0.16 μm to R_a = 0.38 ± 0.02 μm.
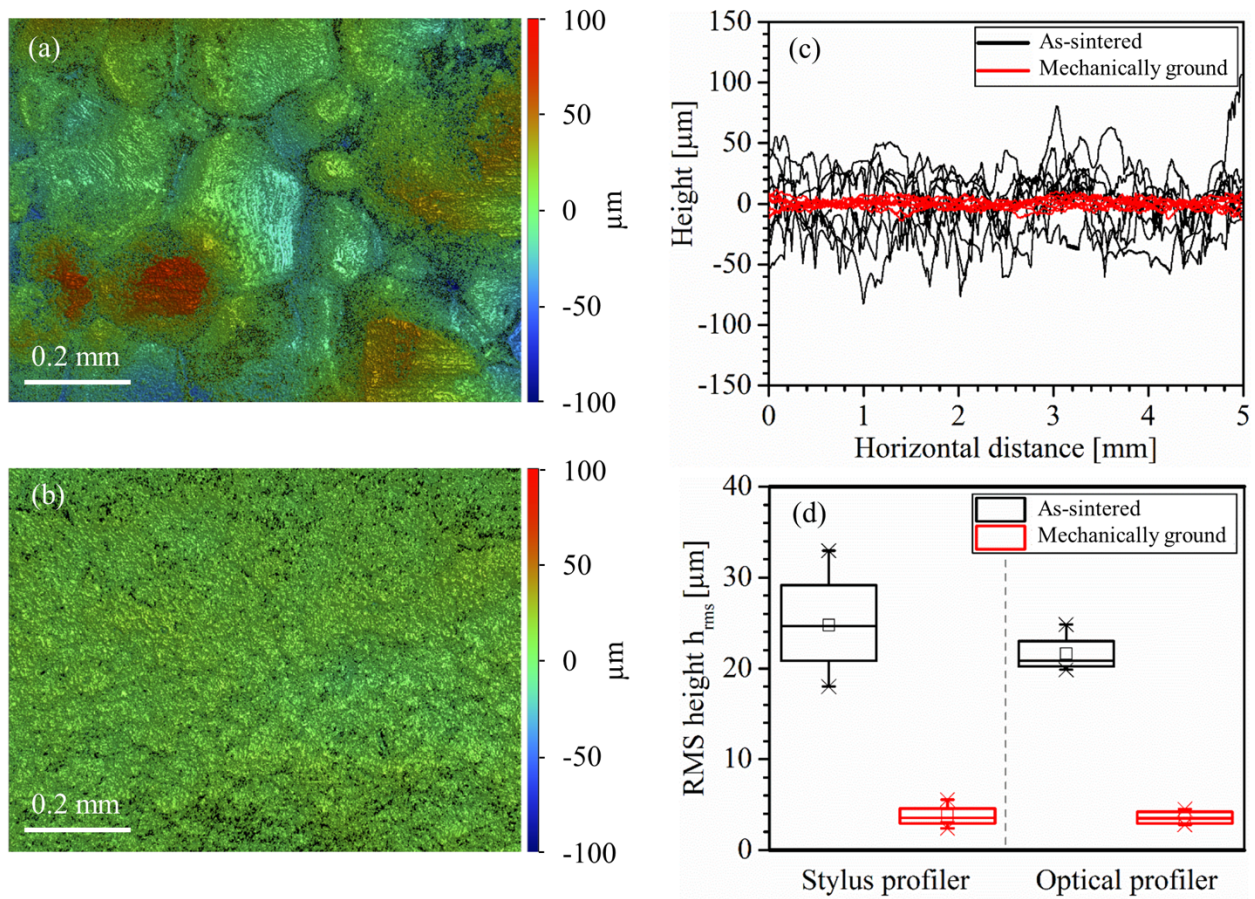

Fig. 7. Optical profilometry was used to collect surface scans of the material in its (a) as-sintered and (b) and mechanically ground state. (c) Line scans of topography were collected using stylus profilometry. (d) The h_{rms} value is compared between conditions.

The same roughness parameters were computed from the optical profilometry data. The RMS height was reduced from h_{rms} = 21.61 ± 2.21 μm to 3.60 ± 0.78 μm upon mechanical grinding step. The filtered values for the as-sintered material were R_q = 12.01 ± 2.52 μm and R_a = 7.65 ±

13

1.58 µm; for the ground sample, they were $R_q = 2.78 \pm 1.10$ µm and $R_a = 1.45 \pm 0.49$ µm. While these values are directly comparable between conditions using the same technique, they are not necessarily comparable between techniques. Not only does the measurement size vary between the techniques, which affects the measured values [46], but also the techniques are subject to different sources of artifacts and errors. The stylus profilometer is subject to tip-size artifacts, which prevent sampling of deep crevices and small lateral-wavelength features. The optical profilometer is subject to interference effects, which are particularly problematic on rough samples such as these. To gain better insight on how the surface roughness may look at the curved surface for the fatigue samples, cross-sectional observations were carried out on the as-sintered and mechanically ground samples and micrographs were shown in Fig. 8. It was seen that the as-sintered sample has a rough surface with deep crevices while the mechanical grinding process eliminated these features.
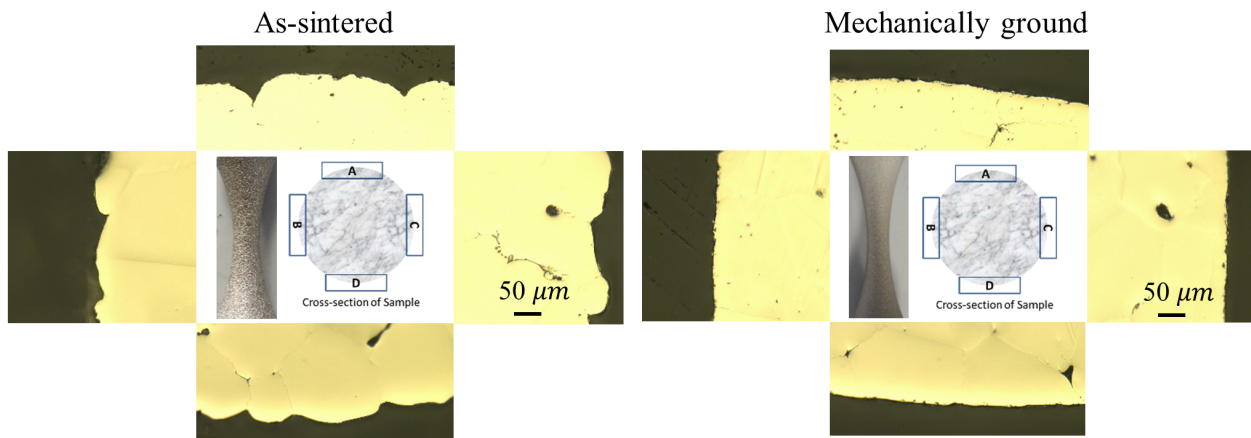

Fig. 8. Optical micrographs taken from the cross-section of the narrowest section of the fatigue sample, where failure is most likely to occur. Comparison shows that the large roughness of the as-sintered sample, which is significantly reduced upon grinding.

The hardness of all samples in the region well below the surface was 225 ± 30 for both samples. The two loads tested, 25 and 50 gf, displayed identical hardness values, therefore the data are averaged together and the typical units ($HV_{0.025}$ and $HV_{0.050}$) are omitted. As expected, the hardness was unaffected by depth for the as-sintered sample. However, the mechanically ground sample displayed a significant increase in the near-surface hardness after grinding, as shown in Fig. 9. Specifically, the hardness at the surface was 415 ± 70, and the increased hardness persisted to approximately 75 µm beneath the surface. This indicates the presence of extensive work hardening in the material from the mechanical grinding step, and likely indicates an increase in surface stress.
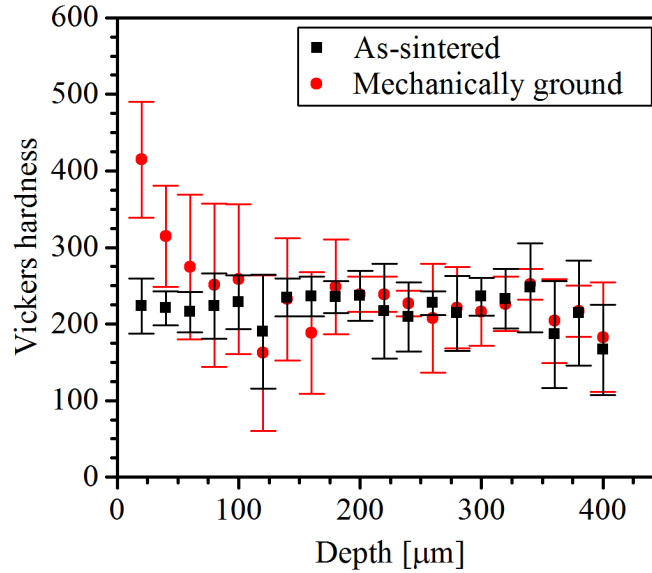
Fig. 9. Hardness measurements on the as-sintered and mechanically ground fatigue samples as a function of depth below the surface of the sample.

To more quantitatively compute the surface stress, XRD of the surface of both as-sintered and mechanically ground samples was performed and results are illustrated in Fig. 10. Comparing the XRD pattern of both surface conditions, two main differences from as-sintered to ground conditions were observed: (1) all peaks shifts to the lower 2θ values and (2) the peaks broadened. Lattice parameters given in Table 2 indicated that peak shift occurred in all peaks and the out-of-plane d-spacing values increased. On the example of the (111) lattice planes, a peak shift from 43.554° to 43.404° was detected from the as-sintered to the mechanically ground condition, respectively. Using Bragg's law, this resulted in an out-of-plane d-spacing value change from 2.076 to 2.083, indicating elastic expansion out-of-plane and compression in-plane. Peak broadening can be inferred as the occurrence of grain refinement and broader micro-strain variations.
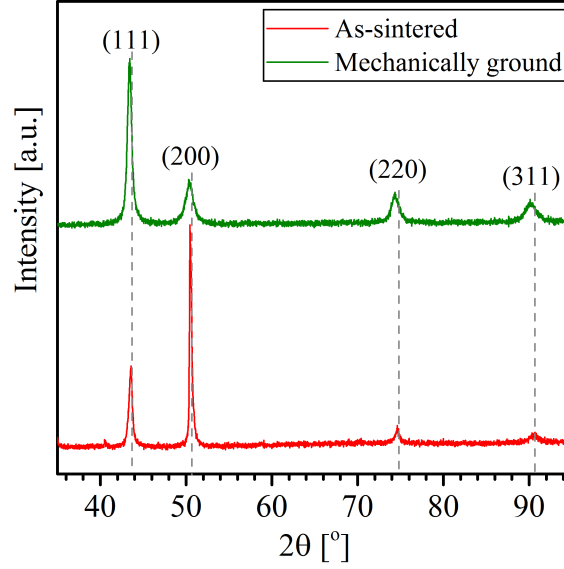
Fig. 10. X-ray diffraction pattern taken from the curved surface of the as-sintered and mechanically ground samples.

Table 2. Crystallographic parameters comparison between as sintered and mechanically ground BJ3DP alloy 625 after sintering process. Units for D-spacing, peak position and FWHM are [Å], [°] and [°], respectively.

Samples	Crystallography parameters											
	111			200			220			311		
	2θ	d-spacing	FWHM	2θ	d-spacing	FWHM	2θ	d-spacing	FWHM	2θ	d-spacing	FWHM
As-sintered	43.560	2.078	0.177	50.438	1.809	0.098	74.669	1.271	0.394	90.520	1.084	0.960
Mechanically ground	43.405	2.085	0.433	50.365	1.812	0.551	74.317	1.276	0.551	90.158	1.088	1.152

The crystallite size and micro-strain of the as-sintered and mechanically ground samples were calculated from line broadening of Bragg diffraction peaks by using the following equations [26]:

$$D = \frac{K\lambda}{\beta} \cos\theta \tag{3}$$

$$\varepsilon = \frac{\beta}{4} \tan\theta \tag{4}$$

where D is the grain/crystallite size, K is a constant, λ is the X-ray wavelength, β is the full width at half maximum (FWHM) of the peak, θ is the Bragg angle of the [h k l] reflection, and ε is the micro-strain. The calculated crystallite size and micro-strain was 483 Å and 0.193% for the as-sintered sample while they were 197 Å and 0.475% for the mechanically ground sample. In other

16

words, a reduction in the grain/crystallite size and increase in the micro-strain was seen after mechanical grinding process, leading to the grain refinement, enhancement of the lattice distortion and increasing micro-strain and, therefore, further contributions to the improved fatigue life of the mechanically ground samples, similar to Refs. [22,24].

3.3 Combining characterization and fatigue results

The fatigue performance of the BJ3DP alloy 625 material is poorer in its as-sintered state as compared to the cast material. However, the performance is significantly improved, even beyond the cast material, upon mechanical grinding. This is true even with a much harsher load-reversal ratio (R = -1 in the present study, as compared to R = 0.1 for the cast material [8]. The optical microscopy, SEM, and μCT data revealed differences in surface roughness between the surface material and bulk material. Hardness measurements showed an enhancement in the surface hardness of the mechanically ground sample. Additionally, XRD revealed crystallite refinement on the surface, in-plane compressive stress, and higher micro-strain due to surface treatment in the mechanically ground sample. These results compare favorably to prior reports on other AM techniques showing effects of surface treatment on fatigue performance in Ti-6Al-4V [47–50] and Ni-based alloys [51,52].

Regarding surface topography, significant reductions in roughness were reflected in all measured roughness parameters, including larger-scale metrics (h_{rms}), smaller-scale metrics (R_q, R_a), and max-/min-height metrics (R_t, R_v). For a given surface stress, some authors [53,54] have proposed phenomenological models linking roughness parameters to notch dimensions, which depend on combinations of metrics such as root-mean-square height, slope, and curvature. However, the values of RMS slope and curvature used in these models depend heavily on small-scale measurement [46] and so cannot be reliably obtained from stylus or optical profilometry.

Finally, the combination of improved surface roughness, microstructural refinement, increased compressive in-plane stress, and micro-strain increases caused by the mechanical surface treatment contributed to the fatigue life enhancement of the BJ3DP alloy 625 samples. Mechanical grinding would therefore be an appropriate tool for all binder-jet printed samples to improve fatigue performance. Further investigation is required to distinguish among these various factors, but the most probable explanation for the significant increase in fatigue performance can be the creation of near-surface mechanical damage and the elimination of deep valleys which serve as stress concentrations.

4. Conclusions

The major aim of the present study was to evaluate binder-jet 3D printing as a technique for creating parts using nickel-based superalloy 625, which maintain high fatigue resistance. Fatigue testing demonstrated poor performance of initially created parts after printing and sintering as compared to prior investigations on the cast material. However, with mechanical grinding of the

surface, the fatigue performance improved significantly, surpassing that of the cast alloy. Fracture surface investigation showed evidence of transgranular crack initiation, followed by intergranular crack growth. µCT and microstructural observations showed that the BJ3DP parts had a relative density of 98.9 ± 0.3 %, with equiaxed grains. The near-surface layer of the as-sintered parts was shown to have unmelted particles, and a layer of increased densification, these surface layers were removed with the mechanical grinding process. Using optical and stylus profilometry, the as-sintered BJ3DP parts were shown to have large roughness, which was significantly reduced upon grinding. The stylus profilometry showed an RMS roughness of $R_q = 1.39 \pm 0.20$ µm, which was reduced upon grinding to $R_q = 0.47 \pm 0.02$ µm. The optical profilometry showed an RMS roughness of $R_q = 12.01 \pm 2.52$ µm, which was reduced to $R_q = 2.78 \pm 1.10$ µm. The differences in these values were attributed to differences in techniques and to measurement artifacts, but both show a significant reduction. The improvement in fatigue behavior likely arose from some combination of: removing the rough surface, micro-strain enhancement, formation of a fine grain structured layer of 75 µm and/or in-plane compressive stress on the surface of the mechanically ground sample. Further work is on-going to distinguish which factor had the most significant effect on fatigue performance. Overall, the present results show that binder jetting, followed by proper sintering and surface treatment, is shown to be a promising alternative to the conventional manufacturing processes for alloy 625.

References

[1]   A. Mostafaei, Y. Behnamian, Y.L. Krimer, E.L. Stevens, J.L. Luo, M. Chmielus, Effect of solutionizing and aging on the microstructure and mechanical properties of powder bed binder jet printed nickel-based superalloy 625, Mater. Des. 111 (2016) 482–491.

[2]   A. Mostafaei, K.A. Kimes, E.L. Stevens, J. Toman, Y.L. Krimer, K. Ullakko, et al., Microstructural evolution and magnetic properties of binder jet additive manufactured Ni-Mn-Ga magnetic shape memory alloy foam, Acta Mater. 131 (2017) 482–490.

[3]   S. Li, Q. Wei, Y. Shi, Z. Zhu, D. Zhang, Microstructure Characteristics of Inconel 625 Superalloy Manufactured by Selective Laser Melting, J. Mater. Sci. Technol. 31 (2015) 946–952.

[4]   P. Ganesh, R. Kaul, C.P. Paul, P. Tiwari, S.K. Rai, R.C. Prasad, et al., Fatigue and fracture toughness characteristics of laser rapid manufactured Inconel 625 structures, Mater. Sci. Eng. A. 527 (2010) 7490–7497.

[5]   K. Amato, Comparison of Microstructures and Properties for a Ni-Base Superalloy (Alloy 625) Fabricated by Electron Beam Melting, J. Mater. Sci. Res. 1 (2012) 3-41.

[6]   F.A. List, R.R. Dehoff, L.E. Lowe, W.J. Sames, Properties of Inconel 625 mesh structures grown by electron beam additive manufacturing, Mater. Sci. Eng. A. 615 (2014) 191–197.

[7]   M. Ziaee, E.M. Tridas, N.B. Crane, Binder-Jet Printing of Fine Stainless Steel Powder with Varied Final Density, Jom. 69 (2017) 592-596.

[8]   A. Theriault, L. Xue, J.R. Dryden, Fatigue behavior of laser consolidated IN-625 at room and elevated temperatures, Mater. Sci. Eng. A. 516 (2009) 217–225.

[9]   A. Mostafaei, E. Stevens, E. Hughes, S. Biery, C. Hilla, M. Chmielus, Powder bed binder jet printed alloy 625: densification, microstructure and mechanical properties, Mater. Des. 108 (2016) 126–135.

[10]   A. Mostafaei, E.T. Hughes, C. Hilla, E.L. Stevens, M. Chmielus, Data on the densification during sintering of binder jet printed samples made from water- and gas-atomized alloy 625 powders, Data Br. 10 (2016) 116–121.

[11]   P. Nandwana, A.M. Elliott, D. Siddel, A. Merriman, W.H. Peter, S.S. Babu, Powder bed binder jet 3D printing of Inconel 718: Densification, microstructural evolution and challenges, Curr. Opin. Solid State Mater. Sci. 12 (2017) 1–12.

[12]   M.P. Paranthaman, C.S. Shafer, A.M. Elliott, D.H. Siddel, M.A. McGuire, R.M. Springfield, et al., Binder Jetting: A Novel NdFeB Bonded Magnet Fabrication Process, Jom. 68 (2016) 1978–1982.

[13]   A. Mostafaei, J. Toman, E.L. Stevens, E.T. Hughes, Y.L. Krimer, M. Chmielus, Microstructural evolution and mechanical properties of differently heat-treated binder jet printed samples from gas- and water-atomized alloy 625 powders, Acta Mater. 124 (2017) 280–289.

[14]   Y. Behnamian, A. Mostafaei, A. Kohandehghan, B.S. Amirkhiz, D. Serate, Y. Sun, et al., A comparative study of oxide scales grown on stainless steel and nickel-based superalloys in ultra-high temperature supercritical water at 800°C, Corros. Sci. 106 (2016) 188–207.

[15]   G.P. Dinda, A.K. Dasgupta, J. Mazumder, Laser aided direct metal deposition of Inconel 625 superalloy: Microstructural evolution and thermal stability, Mater. Sci. Eng. A. 509 (2009) 98–104.

[16]   P. Slebodnickb, E.D. Thomasb, Seawater corrosion behavior of laser surface modified Inconel 625 alloy, 206 (1996) 138–149.

[17]   Q. Guo, Y. Li, J. Qian, H. Yu, C. Chen, Study of the pitting corrosion at welding joints of Inconel 625 alloy under high temperature and high H_2S/CO_2 partial pressure, 12 (2017) 8943.

[18]   H.R.Z. Rajani, S.A.A.A. Mousavi, Materials Science & Engineering A The effect of explosive welding parameters on metallurgical and mechanical interfacial features of Inconel 625/plain carbon steel bimetal plate, Mater. Sci. Eng. A. 556 (2012) 454–464.

[19]   J.D. Lane, T. Riley, T. Riley, Effect of niobium on marine crevice corrosion resistance of Inconel alloy 625 Effect of niobium on marine crevice corrosion resistance of Inconel alloy 625, 599 (2016) 2–7.

[20]   J. Chen, J. Wang, B. Chen, F. Yan, J. Chen, J. Wang, et al., Tribocorrosion Behaviors of Inconel 625 Alloy Sliding against 316 Steel in Seawater, 54 (2011) 514-522.

[21]   L. Sexton, S. Lavin, G. Byrne, A. Kennedy, Laser cladding of aerospace materials, 122 (2002) 63–68.

[22]   O. Unal, E. Maleki, R. Varol, Effect of severe shot peening and ultra-low temperature plasma nitriding on Ti-6Al-4V alloy, Vacuum. 150 (2018) 69–78.

[23]   A. Azhari, C. Schindler, K. Hilbert, C. Godard, E. Kerscher, Influence of waterjet peening and smoothing on the material surface and properties of stainless steel 304, Surf. Coatings Technol. 258 (2014) 1176–1182.

[24]   O. Unal, R. Varol, Surface severe plastic deformation of AISI 304 via conventional shot peening, severe shot peening and repeening, Appl. Surf. Sci. 351 (2015) 289–295.

[25]   K. Zhan, C.H. Jiang, V. Ji, Uniformity of residual stress distribution on the surface of S30432 austenitic stainless steel by different shot peening processes, Mater. Lett. 99 (2013) 61–64.

[26]   S. Dai, Y. Zhu, Z. Huang, Microstructure evolution and strengthening mechanisms of pure titanium with nano-structured surface obtained by high energy shot peening, Vacuum. 125 (2016) 215–221.

[27]   M. Chen, H. Liu, L. Wang, C. Wang, K. Zhu, Z. Xu, et al., Evaluation of the residual stress and microstructure character in SAF 2507 duplex stainless steel after multiple shot peening process, Surf. Coatings Technol. 344 (2018) 132–140.

[28]   P.W. Trester, J.L. Kaae, R. Gallix, Fatigue strength of inconel 625 plate and weldments used in the DIII-D configuration vacuum vessel, J. Nucl. Mater. 133–134 (1985) 347–350.

[29]   L. Mataveli Suave, J. Cormier, D. Bertheau, P. Villechaise, A. Soula, Z. Hervier, et al., High temperature low cycle fatigue properties of alloy 625, Mater. Sci. Eng. A. 650 (2016) 161–170.

[30]   J.F. Grubb, Fatigue Resistance of Alloy 625 Sheet, Miner. Met. Mater. Soc. (1997) 629–637.

[31]   P. Edwards, M. Ramulu, Fatigue performance evaluation of selective laser melted Ti-6Al-4V, Mater. Sci. Eng. A. 598 (2014) 327–337.

[32] A. Taube, A. Kurtovic, T. Niendorf, T. Mertens, C. Zinn, M. Schaper, et al., Influence of surface pre-treatments on the high-cycle fatigue behavior of Ti – 6Al – 4V – From anodizing to laser-assisted techniques, Int. J. Fatigue. 91 (2016) 195–203.

[33] J. G nther, D. Krewerth, T. Lippmann, S. Leuders, T. Tröster, A. Weidner, et al., Fatigue life of additively manufactured Ti-6Al-4V in the very high cycle fatigue regime, Int. J. Fatigue. 94 (2016) 236–245.

[34] J.J. Lewandowski, M. Seifi, Metal Additive Manufacturing: A Review of Mechanical Properties, Annu. Rev. Mater. Res. 46 (2016) 151–186.

[35] Z. Baicheng, L. Xiaohua, B. Jiaming, G. Junfeng, W. Pan, S. Chen-nan, et al., Study of selective laser melting (SLM) Inconel 718 part surface improvement by electrochemical polishing, Mater. Des. 116 (2017) 531–537.

[36] M.N. Islam, S. Sacks, An experimental investigation into the dimensional error of powder-binder three-dimensional printing, Int. J. Adv. Manuf. Technol. 82 (2016) 1371–1380.

[37] M. Doyle, K. Agarwal, W. Sealy, K. Schull, Effect of Layer Thickness and Orientation on Mechanical Behavior of Binder Jet Stainless Steel 420 + Bronze Parts, Procedia Manuf. 1 (2015) 251-262.

[38] D. Hong, D.T. Chou, O.I. Velikokhatnyi, A. Roy, B. Lee, I. Swink, et al., Binder-jetting 3D printing and alloy development of new biodegradable Fe-Mn-Ca/Mg alloys, Acta Biomater. 45 (2016) 375–386.

[39] S. Ahn, S.J. Park, S. Lee, S. V. Atre, R.M. German, Effect of powders and binders on material properties and molding parameters in iron and stainless steel powder injection molding process, Powder Technol. 193 (2009) 162–169.

[40] A. Mostafaei, C. Hilla, E.L. Stevens, P. Nandwana, A.M. Elliott, M. Chmielus, Comparison of characterization methods for differently atomized nickel-based alloy 625 powders, Powder Technol. 333 (2018) 180–192.

[41] I. Ayesta, B. Izquierdo, O. Flaño, J.A. Sánchez, J. Albizuri, R. Avilés, Influence of the WEDM process on the fatigue behavior of Inconel 718, Int. J. Fatigue. 92 (2016) 220–233.

[42] Ö. Özg n, H. Özkan G lsoy, R. Yilmaz, F. Findik, Injection molding of nickel based 625 superalloy: Sintering, heat treatment, microstructure and mechanical properties, J. Alloys Compd. 546 (2013) 192–207.

[43] Q. Bader, E.K. Njim, Effect of Stress Ratio and V Notch Shape on Fatigue Life in Steel Beam, Int. J. Sci. Eng. Res. 5 (2014) 1145–1154.

[44] F.C. Campbell, Fatigue and fracture: understanding the basics. ASM International., 2012.

[45] Fatigue - ASM International, Elements of Metallurgy and Engineering Alloys, Chapter 14 (2008) 243–265.

[46] T.D. Jacobs, T. Junge, L. Pastewka, Quantitative characterization of surface topography using spectral analysis, Surf. Topogr. Metrol. Prop. 5 (2017) 13001.

[47] M. Benedetti, M. Cazzolli, V. Fontanari, M. Leoni, Fatigue limit of Ti6Al4V alloy produced by Selective Laser Sintering, Procedia Struct. Integr. 2 (2016) 3158–3167.

[48] P. Li, D.H. Warner, A. Fatemi, N. Phan, Critical assessment of the fatigue performance of additively manufactured Ti-6Al-4V and perspective for future research, Int. J. Fatigue. 85 (2016) 130–143.

[49] D. Greitemeier, C. Dalle Donne, F. Syassen, J. Eufinger, T. Melz, Effect of surface roughness on fatigue performance of additive manufactured Ti–6Al–4V, Mater. Sci. Technol. 32 (2016) 629–634.

[50] S. Leuders, M. Thone, A. Riemer, T. Niendorf, T. Troster, H. Richard, et al., On the mechanical behaviour of Titanium alloy Ti-6Al-4V manufactured by Selective Laser Melting: fatigue resistance and crack growth performance, Int. J. Fatigue. 48 (2012) 300–307.

[51] O. Scott-Emuakpor, J. Schwartz, T. George, C. Holycross, C. Cross, J. Slater, Bending fatigue life characterisation of direct metal laser sintering nickel alloy 718, Fatigue Fract. Eng. Mater. Struct. 38 (2015) 1105–1117.

[52] S. Gribbin, J. Bicknell, L. Jorgensen, I. Tsukrov, M. Knezevic, Low cycle fatigue behavior of direct metal laser sintered Inconel alloy, Int. J. Fatigue. 93 (2016) 156–167.

[53] D. Arola, M. Ramulu, An examination of the effects from surface texture on the strength of fiber reinforced plastics, J. Compos. Mater. 33 (1999) 102–123.

[54] M. Suraratchai, J. Limido, C. Mabru, R. Chieragatti, Modelling the influence of machined surface roughness on the fatigue life of aluminium alloy, Int. J. Fatigue. 30 (2008) 2119–2126.

Supplementary Information for:
## "Characterizing surface finish and fatigue behavior in binder-jet 3D-printed nickel-based superalloy 625"

Amir Mostafaei [1,†], S. Harsha Vardhan R. Neelapu [1], Cameron Kisailus [1], Lauren M. Nath [1], Tevis D.B. Jacobs [1], Markus Chmielus [1,*]

[1] Department of Mechanical Engineering and Materials Science, University of Pittsburgh, Pittsburgh, PA 15261, USA

[†] Current address: Department of Materials Science and Engineering, Carnegie Mellon University, Pittsburgh, PA, 15213, USA

* Corresponding author:
Email addresses: amir.mostafaei@pitt.edu (A. Mostafaei), chmielus@pitt.edu (M. Chmielus).
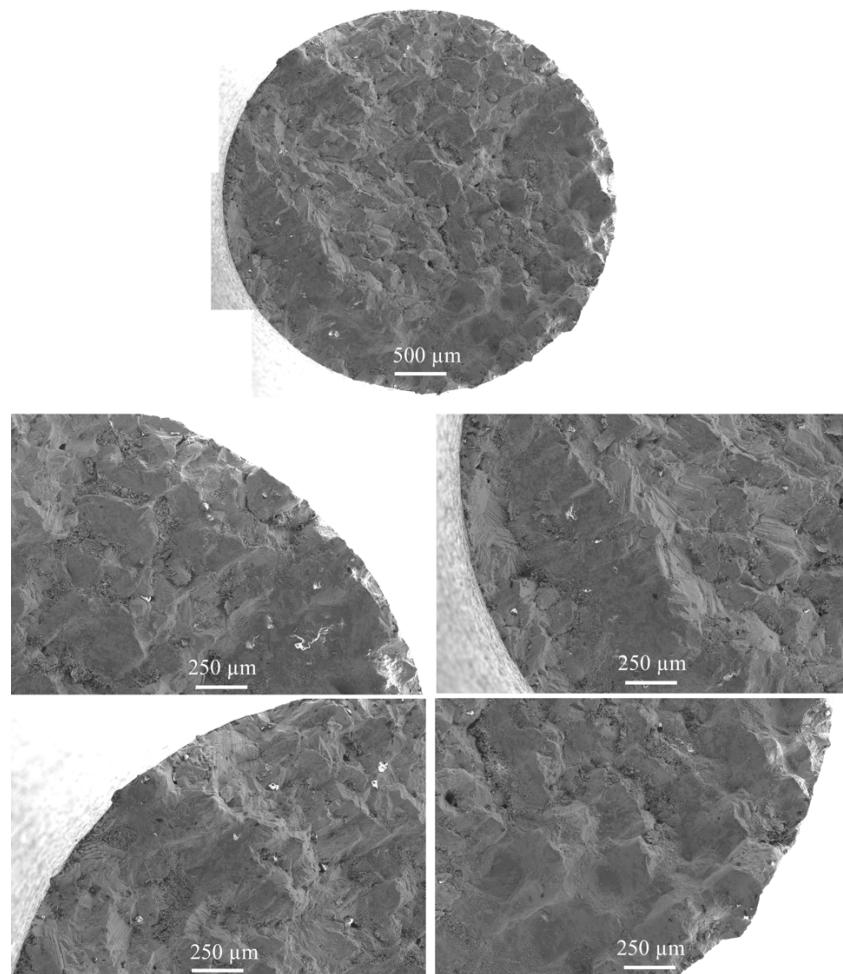
Supplementary Fig. 1. Fracture surface study taken from the mechanically ground sample at the applied stress value of 300 MPa. One fracture mode of transgranular (TG) fatigue fracture failure is seen. Different magnifications indicate regions with different features such as brittle (white arrows) and possibly ductile fractures.